

This is an electronic reprint of the original article. This reprint may differ from the original in pagination and typographic detail.

---

## Functional Lignin Nanoparticles with Tunable Size and Surface Properties: Fabrication, Characterization, and Use in Layer-by-Layer Assembly

Alipoormazandarani, Niloofar; Bensselfelt, Tobias; Wang, Luyao; Wang, Xiaoju; Xu, Chunlin; Willför, Stefan; Fatehi, Pedram

*Published in:*  
ACS Applied Materials & Interfaces

*DOI:*  
[10.1021/acsami.1c03496](https://doi.org/10.1021/acsami.1c03496)

Published: 09/06/2021

*Document Version*  
Accepted author manuscript

*Document License*  
Publisher rights policy

[Link to publication](#)

*Please cite the original version:*

Alipoormazandarani, N., Bensselfelt, T., Wang, L., Wang, X., Xu, C., Willför, S., & Fatehi, P. (2021). Functional Lignin Nanoparticles with Tunable Size and Surface Properties: Fabrication, Characterization, and Use in Layer-by-Layer Assembly. *ACS Applied Materials & Interfaces*, 13(22), 26308-26317. <https://doi.org/10.1021/acsami.1c03496>

### General rights

Copyright and moral rights for the publications made accessible in the public portal are retained by the authors and/or other copyright owners and it is a condition of accessing publications that users recognise and abide by the legal requirements associated with these rights.

### Take down policy

If you believe that this document breaches copyright please contact us providing details, and we will remove access to the work immediately and investigate your claim.

# Functional lignin nanoparticles with tunable size and surface properties: Fabrication, characterization, and use in Layer-by-Layer assembly

*NILOOFAR ALIPOORMAZANDARANI,<sup>a,b</sup> TOBIAS BENSELFELT,<sup>c</sup> LUYAO WANG,<sup>b</sup> XIAOJU WANG,<sup>b</sup> CHUNLIN XU,<sup>b</sup> LARS WÅGGERG,<sup>c</sup> STEFAN WILLFÖR,<sup>b</sup> PEDRAM FATEHI<sup>a,d\*</sup>*

<sup>a</sup> Department of Chemical Engineering, Lakehead University, Thunder Bay, ON, Canada

<sup>b</sup> Laboratory of Natural Materials Technology, Åbo Akademi University, Turku, Finland

<sup>c</sup> Department of Fiber and Polymer Technology, Division of Fibre Technology and Wallenberg Wood Science Center, KTH Royal Institute of Technology, Stockholm, Sweden

<sup>d</sup> State Key Laboratory of Biobased Material and Green Papermaking, Qilu University of Technology, Jinan, Shangdong, China

## ABSTRACT

Lignin is the richest source of renewable aromatics and has immense potential for replacing synthetic chemicals. The limited functionality of lignin is, however, challenging for its potential use, which motivates research for creating advanced functional lignin-derived materials. Here, we present an aqueous-based acid precipitation method for preparing functional lignin nanoparticles (LNPs) from carboxymethylated or carboxypentylated lignin. We observe that the longer grafted side chains of carboxypentylated lignin allow for the formation of larger LNPs. The functional nanoparticles have high tolerance against salt and aging time and well-controlled size distribution

with  $R_h \leq 60$  nm over a pH range of 5-11. We further investigate the layer-by-layer (LbL) assembly of the LNPs and poly (allylamine hydrochloride) (PAH) using a stagnation point adsorption reflectometry (SPAR) and Quartz crystal microbalance with dissipation (QCM-D). Results demonstrate that LNPs made of carboxypentylated lignin (i.e., PLNPs with the adsorbed mass of  $3.02 \text{ mg/m}^2$ ) form a more packed and thicker adlayer onto the PAH surface compared to those made of carboxymethylated lignin (i.e., CLNPs with the adsorbed mass of  $2.51 \text{ mg/m}^2$ ). Theoretical flux,  $J$ , and initial rate of adsorption,  $(\frac{d\Gamma}{dt})_0$ , analyses confirm that 22% of PLNPs and 20% of CLNPs arriving at the PAH surface is adsorbed. The present study provides a feasible platform for engineering LNPs with a tunable size and adsorption behavior, which can be adapted in bionanomaterial production.

KEYWORDS: lignin nanoparticle, PAH, film, SPAR, QCM, adsorption, interface.

## INTRODUCTION

Global environmental and climate challenges call for renewable alternatives to replace fossil-based materials used in various industries. Lignin, extracted from lignocellulosic biomass, is the richest source of renewable aromatics and contains numerous functional groups, such as aliphatic and phenolic hydroxyl groups, which promote the functionalization of lignin for producing lignin-derived materials. Thus, it carries immense potential as a sustainable feedstock for replacing synthetic chemicals.<sup>1,2</sup>

Despite the progress in lignin production, the efficient conversion of lignin into value-added materials is still challenging due to its heterogeneous structure and poor miscibility with other polymeric materials.<sup>3,4</sup> To address this problem, lignin nanoparticles (LNPs) have been recognized as starting materials to form functional materials. These emerging materials have been implemented in different applications, such as UV barriers,<sup>5</sup> nanocomposite reinforcement,<sup>6</sup> drug

delivery and release<sup>7,8</sup> or adsorbent for methylene blue and rhodamine dyes,<sup>9</sup> phosphates,<sup>10</sup> nickel (II) and cadmium (II) ions,<sup>11</sup> and proteins.<sup>12</sup> Compared to the other biodegradable polymers, LNPs may have broader use in biomedical, emulsion, cosmetic, and composite applications due to their higher anti-UV and antioxidant properties as well as better miscibility with other polymers.<sup>13</sup> Lignin nanoparticles are reported to have a size range of 5-500 nm and mostly uniform spherical, hollow and square shapes.<sup>14</sup> Among them, the spherical shape LNPs is preferred, as the spherical-shaped particles do not have sharp edges, which protect particles from breakage during composite, adhesive, or coating formulation processes.<sup>13</sup> In this work, we focus on the formation of LNPs with a uniform spherical shape.

LNPs are fabricated through precipitation procedures initiated by acids, solvent exchange, water-in-oil microemulsion, or sonication methods.<sup>15</sup> Among the mentioned techniques, acid-induced precipitation in ethylene glycol,<sup>16</sup> sodium p-toluenesulfonate,<sup>17</sup> or acetone<sup>18</sup> is the most cost-effective method. Despite this progress, acid-induced precipitation in aqueous systems is more preferred by the industry due to its simplicity and limited environmental footprint. In this study, we present an aqueous acidification system to produce LNPs.

In addition, the generation of functional LNPs was also reported in the past. In one study, lignin nanoparticles were produced in a solvent/antisolvent system (acetone and water) and then coated with a cationic polyelectrolyte to produce cationic LNPs.<sup>11</sup> Alternatively, LNPs were generated in a solvent (ethylene glycol) and antisolvent (i.e., water) system and then chemically esterified or etherified.<sup>12</sup> Similarly, LNPs were generated from lignin-2-(diethyl-amino) ethyl methacrylate (DEAEMA) polymer following a CO<sub>2</sub>/N<sub>2</sub> switchable dispersion/precipitation procedure.<sup>16</sup> These materials have been reported to act as functionalized nanofillers and surfactants in CO<sub>2</sub>/N<sub>2</sub> switchable Pickering emulsions.<sup>19,20</sup> However, designing LNPs with tunable particle size and

functionality is a rather unexplored area. Previous investigations suggest that the alkyl chain length of the covalently attached group of polymers plays an important role in their structural arrangement, orientation, packing behavior.<sup>21-24</sup> To address the proposed research gap, we present a new method for fabricating LNPs from carboxymethylated or carboxypentylated lignin.

The development of polyelectrolyte layer-by-layer assembly has been established as a method to alter the interfacial properties of materials in different systems.<sup>25</sup> As such, poly (allylamine hydrochloride), PAH, has extensively been used for improving paper strength,<sup>26</sup> coating nanoparticles<sup>27</sup>, and preparing xyloglucan<sup>28</sup> and xylan derived coating and binder formulations.<sup>29</sup> However, there is limited understanding of the key parameters controlling the formation of the nanostructured films constituting PAH and functional LNPs. In this case, the surface properties and the adsorption/interaction behavior of functional lignin nanoparticles with the different grafted alkyl side chains have not yet been studied. Considering the sparse available literature, we have investigated the influence of LNPs produced from carboxyalkylated lignin with different carbon spacers (i.e., chain lengths) and studied their adsorption behavior at solid-liquid interfaces in layer-by-layer assembly. This knowledge extends the application range and the commercial utilization of LNPs in different fields, such as surface coating formulations where wet adhesion and interfacial bonding of nanomaterials are of great importance.<sup>27</sup>

## **EXPERIMENTAL DETAILS**

**Materials and Methods.** Analytical grades of sodium chloride (NaCl), sodium dodecyl sulfonate (SDS), poly(diallyl dimethylammonium chloride) (PDADMAC), sodium nitrate, uranyl acetate, poly(ethylene oxide), sodium hydroxide (NaOH), endo-N-hydroxy-5-norbornene-2,3-dicarboxylic acid imide (eHNDI), chromium (II) acetylacetonate, dimethylformamide (DMF), isopropyl alcohol, 6-chlorohexanoic acid (CHA), 2-chloro-4,4,5,5-tetramethyl-1,3,2-

dioxaphospholane, pyridine, sodium chloroacetate (SCA), dimethyl sulphate 98.0% DMSO-d<sub>6</sub>, D<sub>2</sub>O isotopic purity (99.8%), and hydrochloric acid (HCl) were provided by Sigma Aldrich company. Cellulose acetate membrane dialysis tubes with a molecular weight cut-off of 1000 g/mol were supplied by Spectrum Labs. Inc. HPLC grade water was produced by a Milli-Q water purifier and used in all experiments. Silicon wafers used for reflectometry measurements were boron-doped with a thickness of 610-640 μm supplied by Addison Engineering Inc. (single-side polished, San Jose, CA, US). The wafers were washed with Milli-Q water, ethanol, and water, dried with nitrogen gas, and oxidized at 1000 °C for 1 h to form SiO<sub>2</sub>, which was followed by hydrophilization in 10 wt% NaOH and finally cleaned with oxygen plasma (PCD 002, Harrick Scientific Corp., Ossining, NY, US) for 2 min before use. Silica strips (10 × 50 mm) were used as reflectometry substrates. QCM-D crystal sensors with a top layer of silicon oxide were supplied by the Q-Sense, Biolin, Gothenborg, Sweden. Before measurements, silica sensors were cleaned with the SDS solution in Milli-Q water (1wt %) for 5 min at 60 °C and extensively rinsed with Milli-Q water. The sensors were further nitrogen dried and cleaned by a UV/ozone oxidation cleaner (NOVASCAN PSD Series, digital UV ozone system) for another 10 min before use. Poly (allylamine hydrochloride) (PAH) with the weight average molecular weight,  $M_w$ , of 100,000 g/mol was obtained from Alfa Aesar.

Different protocols have been developed to extract lignin from lignocellulosic biomass.<sup>30</sup> Recently, the novel treatment of biomass with the aid of formic acid was used as a techno-economic biorefinery platform to fractionate biomass.<sup>31-33</sup> In this work, lignin, which was extracted via the formic acid treatment of bamboo chips, was produced following a previously described protocol.<sup>34</sup>

### **Production of Carboxymethylated and Carboxypentylated Lignin.**

The scheme of carboxymethylation and carboxypentylation of lignin is shown in Figure S1a. Lignin was carboxymethylated by the SCA reagent following the method described by Konduri.<sup>35</sup> Briefly, 60 mL of lignin solution was prepared at 16 g/L concentration in a three-neck glass flask. The solution was kept in an alkaline medium at pH 11 via adding 2 mL of NaOH (concentration 1 M) at room temperature under constant stirring until fully dissolved. Then, SCA was reacted with lignin at the SCA/lignin ratio of 4/1 mol/mol for 240 min at 60 °C. After completion, the reaction medium was neutralized, and the product was dialyzed for 48 h and freeze-dried. Following the procedure described for the carboxypentylation of liginosulfonate,<sup>36,37</sup> 1.5 g of lignin was suspended in a mixture of isopropyl alcohol (45 mL) and 30 wt.% NaOH (12 mL) at 25°C for 30 min. The activated lignin was then reacted with CHA under the condition of 1 mol/mol CHA/lignin for 2 h and 80°C in a three-neck glass flask while stirring at 300 rpm. The product was extensively washed with ethanol/water (40/10, v/v) and recovered by centrifugation (3500 rpm, 10 min). The precipitated product was dissolved in deionized water (50 mL) and purified using membrane dialysis tubes for two days and dried in the oven at 80 °C.

### **Characterization of Carboxymethylated and Carboxypentylated Lignin**

The molecular weight of the lignin was determined after acetylation with acetic anhydride<sup>38</sup> and by gel permeation chromatography (GPC) with a low temperature-evaporative light scattering detector (LT-ELSD, Shimadzu, Japan) according to the procedure described by Zhang et al.<sup>39</sup>

The charge density, carboxylic acid, and molecular weight of samples were determined as discussed in the supplementary material in Table S1.

Quantitative <sup>31</sup>P NMR spectroscopic analysis of unmodified lignin, carboxymethylated lignin, and carboxypentylated lignin was also performed via phosphitylation (Figure S1b) as reported in the supporting material.

The  $^1\text{H}$  NMR and  $^1\text{H}$ - $^1\text{H}$  COSY NMR spectroscopy analyses of lignin were also performed in  $\text{D}_2\text{O}$  at room temperature via INOVA-500 MHz instrument (Varian, USA). Approximately, 35 mg of unmodified, carboxymethylated, or carboxypentylated lignin were dissolved in 500  $\mu\text{L}$  of  $\text{D}_2\text{O}$ . The acquisition time was set to 3.983 s, and 16 scans with 128 increments and 1 second relaxation time delay.

Furthermore, 0.05 g of oven-dried samples were used for Fourier transform infrared spectrophotometer analysis of samples using Bruker Tensor 37 (Germany, ATR accessory). The spectra were recorded in a transmittance mode in the range of 600-4000  $\text{cm}^{-1}$  with a 4  $\text{cm}^{-1}$  resolution, and 32 scans per sample were conducted.

**Functional Lignin Nanoparticle Production (LNP).** Lignin nanoparticles were formed following the procedure described by Zhang et al.<sup>6</sup> Briefly, 0.1 g of carboxymethylated or carboxypentylated lignin was mixed with 100 mL of milli-Q water, and the pH was increased by adding 0.1 M NaOH under constant stirring (300 rpm) until full dissolution was observed. Then, LNPs were formed by acid precipitation through the addition of 0.1 M HCl to reach the desired pH value. Optimum properties were achieved at pH 6 in this study. Therefore, further characterization and adsorption analysis of nanoparticles was conducted at this pH. The carboxymethylated lignin nanoparticles (with the charge density of -1.85 meq/g), denoted as CLNPs, and carboxypentylated lignin nanoparticles (with the charge density of -1.91 meq/g), denoted as PLNPs, were used in this analysis. Unmodified lignin nanoparticle was labeled as LNPs.

The reversibility analysis of nanoparticles was studied via alkalizing initially acidified nanoparticles at pH<4 to pH 11 by 0.1 M NaOH and then via acidifying the medium to pH 4 by

0.1 M HCl in 4 cycles. The particle size of the nanoparticles was measured after every cycle at pH 6.

**Characterization of Functional LNPs.** The particle size ( $R_h$ ) and zeta potential ( $\zeta$ -potential) of lignin nanoparticles were analyzed by the dynamic light scattering (DLS) instrument using a Zetasizer Nano series (Malvern Instruments Ltd., UK), which was equipped with a folded capillary cell. Measurements were conducted in triplicates at a concentration of 0.1 wt %. The morphology of LNPs, CLNPs, and PLNPs was imaged using a JEM-1400 Plus transmission electron microscope (TEM, JEOL Ltd., Japan) at 80 kV acceleration voltage. In this experiment, 5  $\mu$ L of diluted LNP dispersions (0.1 mg/ mL) was applied on a formvar/carbon-coated copper grid for 3 min, which was followed by staining with 5  $\mu$ L of uranyl acetate (2 wt%) for 1 min. The stained grid with a uniform nanoparticle layer was then used for TEM imaging.

### **Adsorption Analysis**

**SPAR Analysis.** The amount of adsorbed polyelectrolyte and nanoparticle was determined using stagnation point adsorption reflectometry provided by the Laboratory of Physical Chemistry and Colloidal Science, Wageningen University, Netherlands. The complete description of the method can be found in the report carried out by Dijt et al.<sup>40</sup> and validation of lignin in this model is thoroughly explained elsewhere.<sup>41</sup> Also, the applied procedure is explained briefly in the supplementary material.

In this study, a baseline was formed in Milli-Q water with the same pH and ionic strength as the polyelectrolyte solutions on a clean SiO<sub>2</sub> surface for 5 min. PAH (25 mg/L solutions at pH 6 in salt-free and 10 mM NaCl) was subsequently adsorbed on the surface. Then, lignin nanoparticles (25 mg/L with the same ionic strength and pH as PAH) were adsorbed onto the PAH layer after rinsing to form a multilayer model structure (i.e., silicon, SiO<sub>2</sub>, PAH, LNPs, PAH, LNPs, and

water) as described in Figure S2. In this experiment, the adsorption sequence of PAH-rinse-LNPs-rinse was repeated at a flow rate of 1 mL/min under an ambient environment to form four bilayers. The modeling was performed with the aid of the Professor Huygens software (Dullware, The Netherlands) supplied with the SPAR instrument. A layered optical model was used for calculating the adsorbed amount of polyelectrolyte from the SPAR data. The refractive index increment (dn/dc) of the PAH, CLNPs, and PLNPs were determined to be 0.225 mL/g,<sup>42</sup> 0.193 mL/g, and 0.195 mL/g, respectively (using Brookhaven BI-DNDC differential refractometer, USA).

**QCM-D Studies.** In this work, the adsorption mechanisms of PAH, CLNPs, and PLNPs were studied in a wet state using a QCM-D 401, E1, Q-Sense Inc. Gothenborg, Sweden. Adsorption was conducted using a clean silicon oxide sensor. CLNPs, PLNPs, and PAH were prepared at 0.1 g/L solutions, 10 mM NaCl, and pH 6. Solutions were pumped by a peristaltic pump at the flow rate of 0.15 mL/min and the temperature was set to 20 °C. Adsorption was initiated by establishing a baseline for 5 min, then PAH was adsorbed on the sensor surface, which was followed by the adsorption of CLNPs or PLNPs. This procedure was repeated to assemble four layers. Buffer rinsing was conducted after every stage of adsorption, and results from the 5<sup>th</sup> overtone were presented. The details of QCM-D principles are described in the supplementary material.

**Trapped Water Mass Fraction and Layer Thickness of Adlayer.** The swelling of adsorbed polymeric films can be calculated by combining the dry mass per unit area,  $\Gamma_{dry}$ , obtained by SPAR, and the wet mass per unit area,  $\Gamma_{wet}$ , obtained by QCM-D analysis. The mass fraction ( $x$ ) of trapped water in the film can be estimated from Equation 1:<sup>42</sup>

$$x = 1 - \frac{\Gamma_{dry}}{\Gamma_{wet}} \quad [1]$$

To determine the thickness of the film theoretically ( $L_{theoretical}$ ), water fraction ( $\phi$ ) of the film is determined from ideal mixing law following equations 2 and 3:

$$\phi = \frac{\rho_p x}{\rho_p x + \rho_s (1-x)} \quad [2]$$

$$L_{theoretical} = \frac{\Gamma_{wet}}{\rho} \quad [3]$$

where  $\rho_s$  is the density of the NaCl solution,  $\rho_p$  is the density of the polyelectrolyte and  $\rho$  is the density of the film. In the present case, PAH and CLNP/PLNPs densities were taken as 1.15 and 1.35 g/cm<sup>3</sup> as reported elsewhere.<sup>43,44</sup> The density of the wet film is given by equation 4:

$$\rho = \rho_p(1 - \phi) + \rho_s \phi \quad [4]$$

**Atomic Force Microscope (AFM).** The surface roughness of multilayer film after the deposition of 4 layers of PAH-LNPs-PAH-LNPs in SPAR was assessed by AFM, MultiMode 8 (Bruker, Santa Barbara, CA, USA) in a dry state in the air at ambient conditions. RTESP 150 cantilevers with the spring constant and tip radius given by the supplier were used in the scanAsyst mode. The surface roughness was determined over an area of 1×1 μm.

**Error Calculations.** All error intervals ( $x \pm \Delta x$ ) were at least 95% confidence calculated from the standard deviation ( $S_x$ ) of repeat measurements ( $N$ ), that is,  $\Delta x = S_x \times t\text{-value} / (N)^{1/2}$ , where the t-value is obtained from t-distribution at a confidence level of 95% for  $N-1$  degrees of freedom.

## RESULTS AND DISCUSSION

**Characterization of Modified Lignin.** Lignin was carboxymethylated and carboxypentylated by SCA and CHA reagents as explained in the material section. The hydroxyl groups of lignin samples were determined via <sup>31</sup>P NMR, and the <sup>31</sup>P NMR spectra of the samples were presented in Figure 1a, while the quantitative data was summarized in Table 1. The modification of lignin resulted in an insignificant change in the aliphatic -OH and some reductions in the total phenolic -OH groups, indicating the phenolic hydroxyl group of lignin as a substitution site for the carboxyalkylation reaction. Furthermore, the concentrations of carboxylate groups in carboxymethylated lignin (1.75

mmol/g) and carboxypentylated lignin (1.71 mmol/g) were higher than that in unmodified lignin (0.47 mmol/g), demonstrating the successful functionalization of lignin.

**Table 1.** Assignment of Different Functional Groups of Lignin Derivatives Determined by  $^{31}\text{P}$  NMR Spectrum.

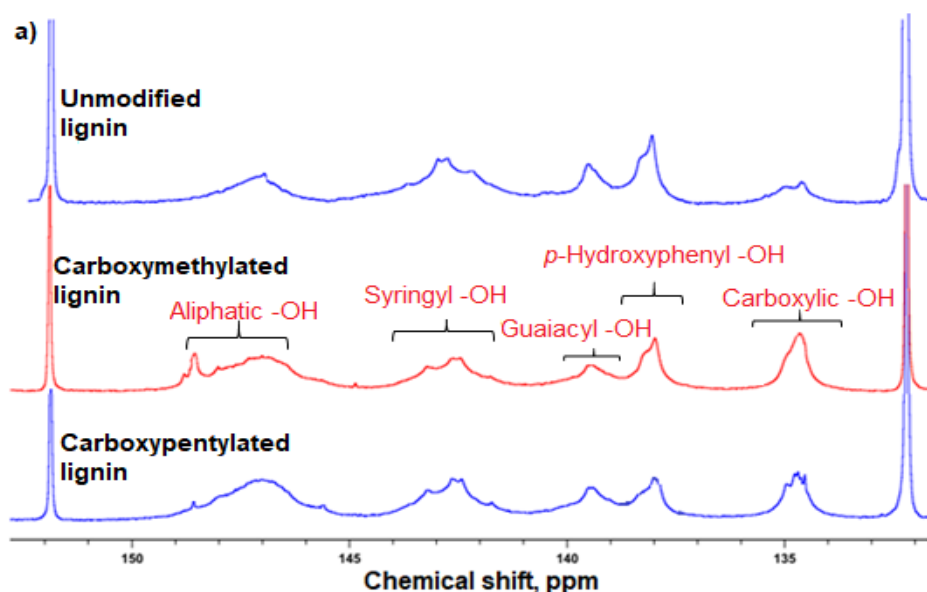
Peak	Chemical shift (ppm)		Unmodified lignin (mmol/g)	Carboxymethylated lignin (mmol/g)	Carboxypentylated Lignin (mmol/g)
1	141.7-143.1	Syringyl -OH	1.71	1.58	1.60
	138.3-140.3	Guaiacyl -OH	1.35	1.02	0.88
	137.3-138.3	<i>p</i> -hydroxyl -OH	1.64	1.20	1.04
		Total phenolic -OH	4.70	3.80	3.52
2	145.5-150.4	Aliphatic -OH	2.68	2.62	2.64
3	134.0-135.9	Carboxylate	0.47	1.75	1.71

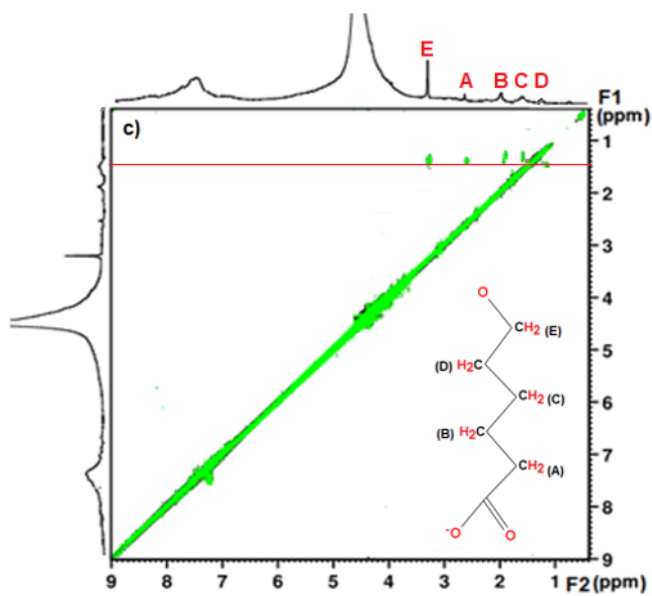
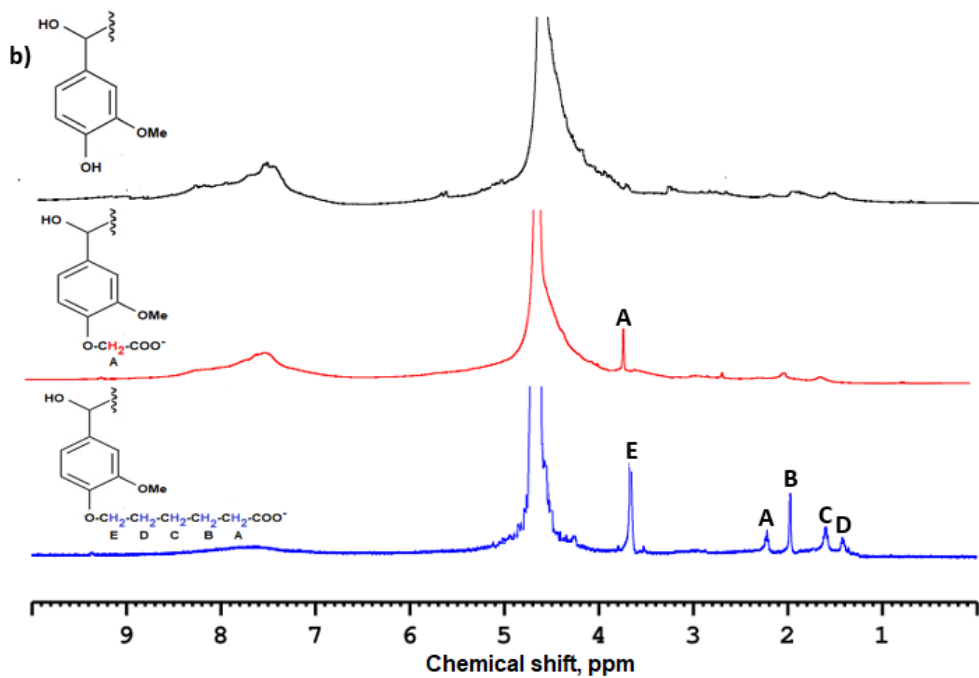
In the  $^1\text{H}$  NMR spectra shown in Figure 1b, the peak at 4.70 ppm corresponds to  $\text{D}_2\text{O}$  solvent, and peaks at 6-8 ppm are attributed to the protons of the aromatic ring.<sup>36,37</sup> The appearance of new signals in the range of  $\delta \approx 1.40\text{-}3.70$  ppm (assigned to the hydrogen of A at 3.70 ppm for carboxymethylated lignin or E at 3.70 ppm, C-D at 1.40-1.55 ppm, B at 2.00 ppm, and A at 2.20 ppm for carboxypentylated lignin (Figure 1b) confirmed the successful grafting of carboxylate groups to the lignin backbone.

$^1\text{H}$ - $^1\text{H}$  COSY NMR was also used for confirming the coupled spins of carboxypentylated lignin (Figure 1c). Several distinct peaks were observed, in which the diagonal peaks centered at  $F_1 \approx F_2 \approx 4.70$  ppm belonged to  $\text{D}_2\text{O}$ . The appearance of four cross-peaks at  $\{F_1 = 1.55 \text{ ppm}, F_2 = 3.70 \text{ ppm}\}$ ,  $\{F_1 = 1.55 \text{ ppm}, F_2 = 2.20 \text{ ppm}\}$ ,  $\{F_1 = 1.55 \text{ ppm}, F_2 = 2.00 \text{ ppm}\}$  and  $\{F_1 = 1.55 \text{ ppm}, F_2 = 1.40$

ppm} in carboxypentylated lignin indicated the coupling of H-A, H-B, H-C, H-D and H-E.<sup>36</sup> The cross-peak of {F<sub>1</sub> = 3.70 ppm, F<sub>2</sub> = 3.70 ppm} overlapped with the diagonal line. The absence of other cross-peaks at 1.40-3.70 ppm confirmed the different chemical structures of carboxymethylated lignin (Figure S1c) and carboxypentylated lignin. The information of the <sup>1</sup>H- and <sup>1</sup>H-<sup>1</sup>H COSY NMR technique provides evidence for the carboxymethyl and carboxypentyl groups on the structure of modified lignin samples.

The FTIR spectra of samples are presented in Figure 1d. As seen, all three lignin samples showed a broad band at 3404 cm<sup>-1</sup>, which is assigned to stretching vibration of phenolic and aliphatic -OH groups.<sup>36,37</sup> Other distinctive peaks related to the unmodified lignin characteristics are explained in the supplementary material. Also, carboxymethylated and carboxypentylated lignin had sharp absorption peaks at 1595 cm<sup>-1</sup> and 1042 cm<sup>-1</sup>, corresponding to C=O and C-O stretching, respectively.<sup>36,37</sup> This observation indicated that modified lignin samples contained considerably more carboxyl groups compared to the unmodified lignin. The molecular weight of unmodified lignin (11300 g/mol) was lower than that of carboxymethylated lignin (28700 g/mol) and carboxypentylated lignin (29900 g/mol), as listed in Table S1.





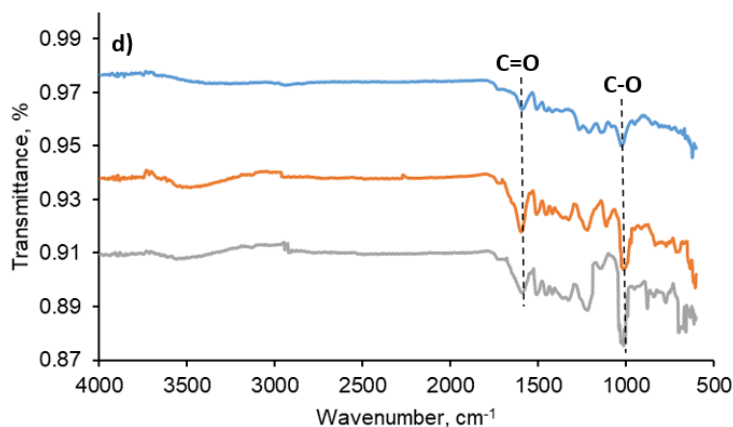


**Figure 1.** a)  $^{31}\text{P}$  NMR spectra of unmodified, carboxymethylated and carboxypentylated lignin, b)  $^1\text{H}$  NMR spectra of unmodified, carboxymethylated, and carboxypentylated lignin, c)  $^1\text{H}$ - $^1\text{H}$  COSY spectrum of carboxypentylated lignin in  $\text{D}_2\text{O}$ , d) FTIR spectra of unmodified lignin, carboxymethylated and carboxypentylated lignin.

**Controlling LNP Formation in Aqueous Solution.** The preparation of LNPs commonly employs organic solvents, such as tetrahydrofuran, ethyl glycol, dimethyl sulfoxide, and acetone.<sup>13</sup> For the industrial viability of this technique, we replaced organic solvents with water. In this study, unmodified lignin, carboxymethylated, and carboxypentylated lignin were fully dissolved in an aqueous system in the presence of NaOH at pH 11. Then, the nanoparticles were formed by acid precipitation through the addition of HCl. The schematic illustration of nanoparticle fabrication is shown in Figure S3a. The effects of concentration and pH on the stability and size of CLNP and PLNP dispersion are discussed in the supplementary material (Figure S3b and S3c). As seen in Figure 2a, high dispersion stability was observed at a pH >4, and the corresponding TEM images of CLNPs and PLNPs in Figure 2a showed their spherical structures (particle size range of 10-60 nm with an unnoticeable difference for CLNPs and PLNPs). The acidification, however, changed the appearance of the dispersions from transparent to opaque at pH <4 (Figure 2a left), which was attributed to the protonation of carboxylic acid at pH <4.

The pH-responsive reversibility of the formed nanoparticles is shown in Figure 2b and the corresponding particle size is reported in Figure S3d. The formation of functional CLNPs and PLNPs remained reversible in the first 2 cycles with minimal particle size variation. After the nanoparticle formation at pH 4, an increase in the pH from 4 to 11 assisted with the nanoparticle reformation in the first two cycles, which was mediated by the carboxylic acids. This process became irreversible after 2 cycles, as observed by the cloudy solution and particle size growth. This is probably due to the loss of nanoparticle functionality via the cleavage of grafted alkyl side chains under strong alkalinity. In the case of LNPs, the particle size increased in all pH cycles due to their lower charge density and water solubility. In other words, LNPs remain agglomerated in the pH reversibility analysis, which shows the importance of the carboxyalkylation to control the formation and stability of the lignin nanoparticles.

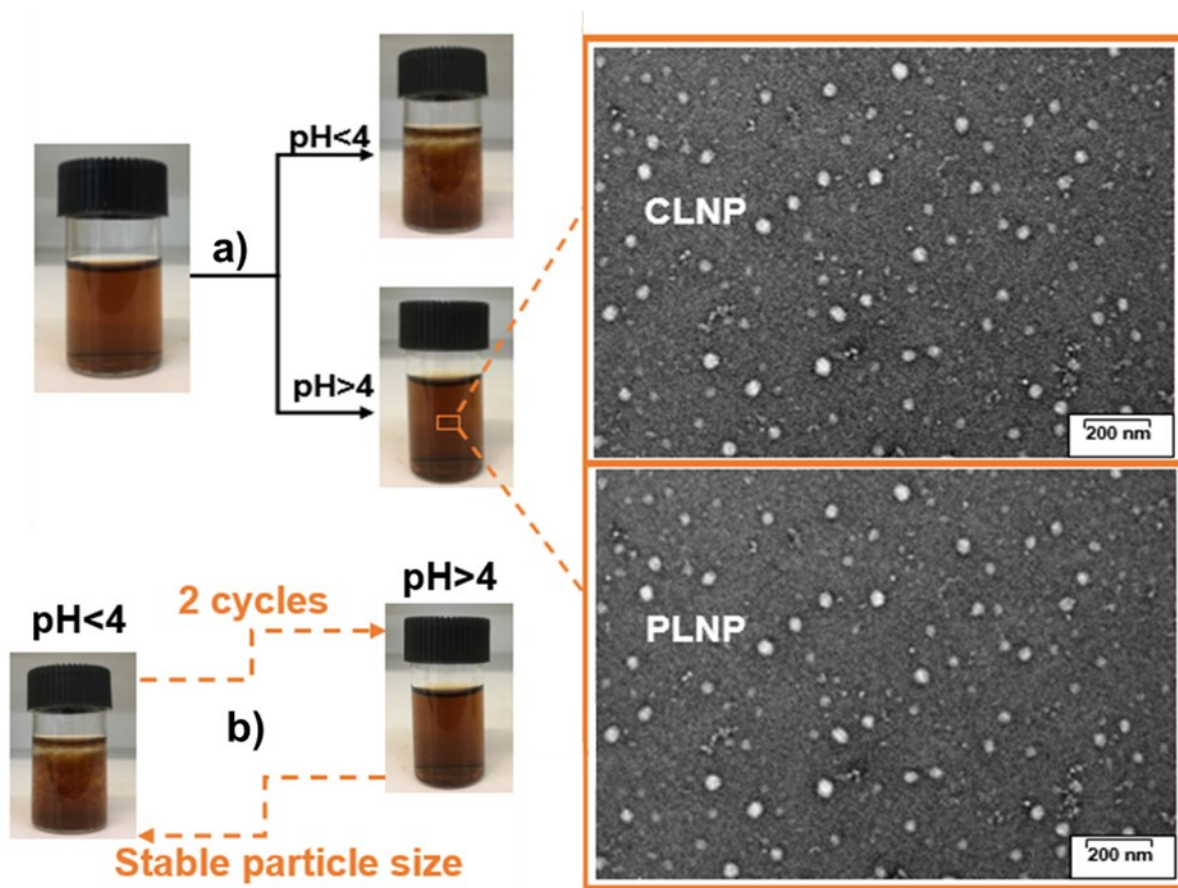


**Figure 2.** a) Illustration of LNP dispersion and corresponding TEM images of CLNPs and PLNPs obtained at pH=6. b) pH-responsive reversibility of nanoparticle formation.

**$\zeta$ -Potential and  $R_h$  of LNP Dispersions.** The colloidal stability of LNPs is important for scale-up and utilization of the materials in different applications. Thus, we characterized LNPs, CLNPs, and PLNPs in terms of  $\zeta$ -potential and particle size ( $R_h$ ). The  $\zeta$ -potential analysis presented in Figure 3a shows that CLNP and PLNP dispersions were stable in the pH range of 5-11, attributing to strong double-layer repulsion between particles.<sup>18</sup> As pH increased to 11, the carboxylate groups on the surfaces were fully disassociated, resulting in a  $\zeta$ -potential of -40 mV for CLNPs and -45 mV for PLNPs. Results highlighted that the negative  $\zeta$ -potential values increased slightly as the grafted chain length increased from one carbon in CLNPs to five carbons in PLNPs, which is

suggested to be due to a lower counterion condensation when charged groups are further apart, as described by the Bjerrum length.<sup>45</sup> The  $\zeta$ -potential of LNPs was lower than that of CLNPs and PLNPs due to the lower concentration of charged groups (Table 1).

The particle size of the CLNPs and PLNPs remained stable with  $R_h \leq 60$  nm in the pH range of 5-11 (Figure 3b). At the initial stage of nanoparticle formation, particles started to self-associate to form a nucleus, which was governed by a balance between electrodynamic and electrostatic forces.<sup>46</sup> Thus, a high available charge in CLNP and PLNP dispersions resulted in a rather smaller nucleus (Figure 3b, schematic illustration), attributing to the enhanced repulsion between the negatively charged groups.<sup>47</sup> Furthermore, longer grafted side chains resulted in less proximity of charged groups, and thus carboxypentylation allowed for the formation of larger nanoparticles. By contrast, the largest  $R_h$  of LNPs indicated that the low-charged lignin with a limited concentration of carboxyl groups coiled to form a larger cluster by van der Waals or  $\pi$ - $\pi$  interactions when there was less repulsion.<sup>48</sup> The aggregation of LNPs was supported by its aggregated fractal structure observed in the TEM image (Figure S4). This is in agreement with the aggregation of lignin derivatives studied by Norgen et al.<sup>48</sup>

Below pH 4, the initially formed nucleus started to agglomerate in the CLNP and PLNP dispersions. Carboxylate groups are predominantly uncharged and protonated at  $\text{pH} < 4$ . Thus, the repulsive interactions induced by charged groups are diminished at this stage. This yielded a more compact and dense assembly of the lignin subunit chains,<sup>47</sup> promoting lignin association owing to Van der Waals attractions.

To evaluate the sensitivity of the lignin nanoparticle dispersion to changes in chemical conditions, we studied the size alteration of the nanoparticles in the dispersion at different ionic strengths (Figure 3c). The  $R_h$  of CLNPs and PLNPs was stable up to 50 mM NaCl (pH 6), and the particles

agglomerated at 500-1000 mM NaCl when the surface charges of functional nanoparticles were screened and van der Waals forces dominated. This observation was also supported by the existence of a clear reduction in the  $\zeta$ -potential shown in Figure S5a and agrees with the DLVO theory, which is explained by a decrease in the osmotic double-layer repulsion when the bulk salt concentration approaches that in the counterion cloud.<sup>49</sup> LNPs also indicated the same stability towards ionic strength variations. The stability of different nanoparticle dispersions was also evaluated as a function of time (Figure S5b), and the results indicated that CLNP and PLNP dispersions were very stable in water with no significant aggregation after 20 days. However, nanoparticle size increased at pH below 4 after 20 days.

From the results discussed above, it can be concluded that CLNPs and PLNPs were considerably more stable than LNPs over a wider pH range and were insensitive to variations in pH ranging from 5 to 11 and ionic strength up to 50 mM. Considering these results and the non-spherical fractal structure of LNPs (Figure S4), we decided to not include LNPs further in this work. By contrast, the excellent colloidal stability of PLNPs and CLNPs is interesting for many applications, for example, coatings formed by multilayer assemblies, which we discussed in the following section.

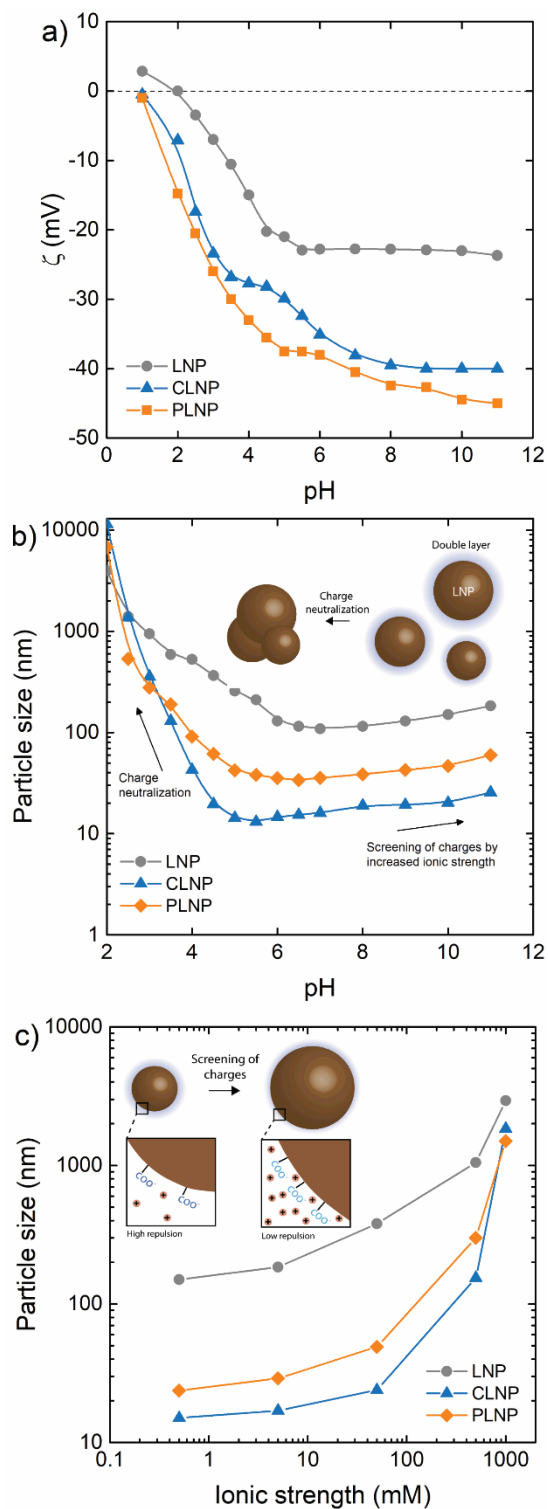


**Figure 3.** a)  $\zeta$ -potential and b) average particle size of lignin nanoparticles as a function of pH in the absence of salt and c) particle size as a function of ionic strength at pH 6.

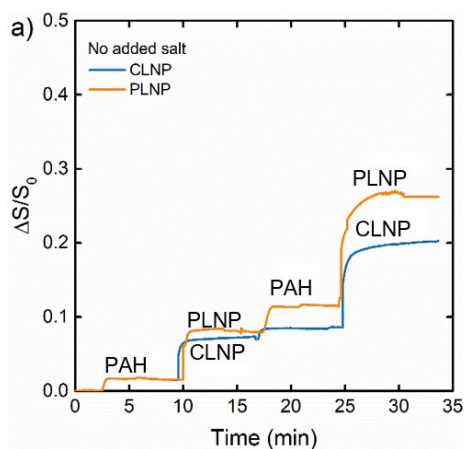
**PAH and CLNP/PLNP Multilayer Formation.** An interesting property of charged nanoparticles is that they can be assembled in the multilayered film using the layer-by-layer assembly technique. Interestingly, lignin nanoparticles can be used to create coatings with UV-blocking or antioxidant properties. We formed multilayers with the lignin nanoparticles by combination with the polycation PAH, and the assembly was studied using SPAR and QCM-D techniques. The SPAR data in Figure 4 shows that a higher adsorbed amount was observed in an electrolyte concentration of 10 mM NaCl (Figure 4b) compared to that in a salt-free system (Figure 4a). It is well-known that an increase in the salt concentration leads to a more coiled conformation of the polyelectrolyte chain and higher adsorption due to larger charge overcompensation.<sup>50</sup> This was previously explained to cause a more pronounced three-dimensional structure of PAH at the interface of SiO<sub>2</sub>,<sup>51</sup> which may partly explain the greater adsorption of CLNPs or PLNPs on PAH at a higher salt concentration. In addition, the adsorption response of CLNPs/PLNPs on PAH to a higher salt concentration is affected by the lignin nanoparticle size at this ionic strength.

We also noted that the kinetics of PAH adsorption is rather fast, reaching saturation within 100 sec upon addition. In this case, smaller and highly charged PAH molecules have a faster adsorption kinetic due to their faster diffusion and easier packing at the surface. CLNPs or PLNPs, on the other hand, exhibited rather slow adsorption at 10 mM salt with saturation times between 200-400 sec. The large size of these particles results in slower diffusion towards the surface. Furthermore, when the surface started to be saturated, there was a significant repulsion and limited space for the following particles to adsorb, which led to a lower adsorption rate due to required rearrangements of the molecules on the surfaces.<sup>52</sup>

The multilayer formation presented in Figure 4 also shows different dynamics for CLNPs and PLNPs. PLNPs with five carbon alkyl side chains have a higher adsorption capacity compared to

CLNPs with one carbon alkyl side chain even though they have a similar degree of modification. This is in agreement with previous reports where polymers having a longer alkyl side chain showed enhanced adsorption properties.<sup>24</sup> PLNPs are larger, and hence they are likely to have a softer and more dynamic charged radiance that yields a better attachment to the PAH surface. Thus, the side chain of nanoparticles is an important factor in nanoparticle adsorption.

The morphology of the multilayer was further evaluated by AFM imaging (Figure 4c,d), which shows a similar structure for CLNPs and PLNPs but with different surface roughness. The images demonstrated that the PAH/PLNP multilayer with higher adsorption had a higher roughness of 3.3 nm (with the corresponding average height of 18 nm), while the CLNP surface had a roughness of 2.9 nm with an average height of 15.7 nm relating to its lower particle size. Moreover, there are some clusters formed on the surface upon the adsorption of both nanoparticles, indicating aggregation upon drying or aggregation in the vicinity of the surface during the adsorption. The seemingly low surface coverage is commonly observed for this type of nanoparticle adsorption.<sup>53</sup>



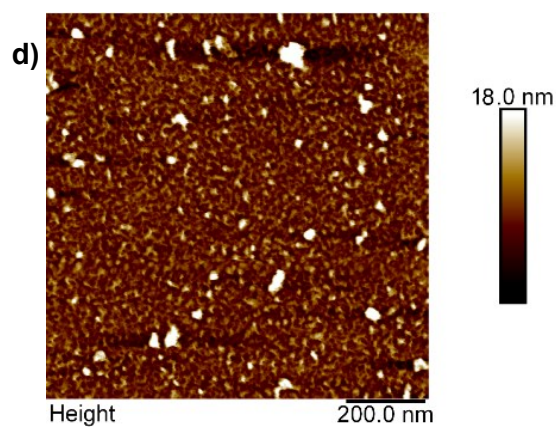
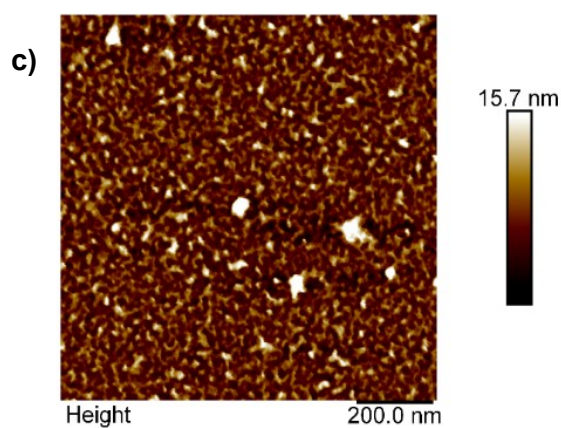
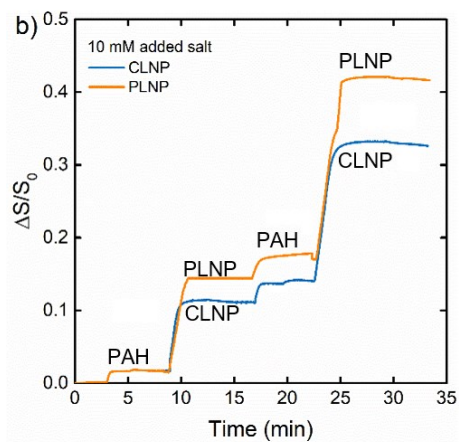


**Figure 4.** SPAR adsorption data showing the reflectometry signal ( $\Delta S/S_0$ ) for the multilayer formation of PAH (the 1<sup>st</sup> and 3<sup>rd</sup> layer) and CLNP/PLNP (the 2<sup>nd</sup> and 4<sup>th</sup> layer) onto SiO<sub>2</sub> surface at a) 0 M NaCl and, b) 10 mM NaCl. The polyelectrolyte concentration is 25 mg/L. AFM images

of 4 multilayers of c) PAH/CLNP, and d) PAH/PLNP onto SiO<sub>2</sub> surfaces using SPAR at 10 mM NaCl and pH 6.

**Quantification of the Adsorbed Amounts in the Adsorbed Layers.** We calculated the dry and wet adsorbed amounts using SPAR and QCM-D (Table 2). PAH adsorption onto silica is governed by ion-exchange interactions between charged silanol groups and partially ionized cationic PAH (approximately 50% protonation at pH 6).<sup>54</sup> Likewise, the ion-exchange interactions are mainly responsible for the adsorption of CLNPs and PLNPs on the PAH saturated surface. Based on the SPAR data, the adsorbed amounts of the first CLNP and PLNP layers on the first PAH layer are 2.51 and 3.02 mg/m<sup>2</sup>, respectively. Based on the charge compensation mechanism involved in the adsorption, the theoretical mass required for neutralizing all available PAH charges on the surface is calculated to be 2.59 mg/m<sup>2</sup> for CLNPs and 2.50 mg/m<sup>2</sup> for PLNPs based on the adsorbed mass of PAH and the charge density of the LNPs (calculation available in the supplementary material). The comparison of required theoretical adsorbed mass to actual adsorbed mass reported in Table 2 explains that the available charges of PAH were compensated for by CLNPs. By contrast, PLNPs induced a significant overcompensation where all PAH were neutralized by the anionic nanoparticles. Thus, alkyl side chain length plays a crucial role in neutralizing the opposite polyelectrolyte charges, and the size leads to a greater overcompensation.

The mass fraction of trapped water in the adsorbed layer is reported in Table 2. PLNPs adsorbed more and had a smaller trapped water mass fraction ( $x_{\text{trapped water}}=0.27\pm 0.01$ ), while CLNPs adsorbed less but contained more trapped water  $x_{\text{trapped water}}=0.30\pm 0.02$ . Therefore, adlayers formed by PLNPs with a longer alkyl side chain are thicker, more packed, and contain slightly less water. However, CLNPs with one carbon side chain induced a thinner and loosely bound adsorbed layer

with a higher water fraction. Moreover, considering the low theoretical adsorbed layer thickness,  $L_{theoretical}$ , and the size of PLNPs and CLNPs, it can be concluded that nanoparticles undergo a substantial conformational rearrangement when depositing on the PAH surface. Results are also in line with the adsorption of poly(styrene sulfonate) with the radius of gyration of 30-100 nm forming a layer thickness of 0.5-2 nm on amino-functionalized silica surface in SPAR studies.<sup>42</sup>

**Table 2.** Data for the CLNP or PLNP adsorption onto PAH-treated SiO<sub>2</sub> surface (adsorbed mass of PAH was  $\Gamma_{SPAR}=0.55$  mg/m<sup>2</sup> and  $\Gamma_{QCM}=0.99$  mg/m<sup>2</sup> and is excluded from the reported values) at 0.1 M NaCl.

	$\Gamma_{QCM}$ mg/m <sup>2</sup>	$\Gamma_{SPAR}$ mg/m <sup>2</sup>	$\Delta m_{Theoretical}$ , mg/m <sup>2</sup>	$x_{trapped}$ water, mg/mg	$L_{Theoretical}$ , nm
CLNP	3.58±0.2	2.51±0.1	2.59	0.30±0.01	2.93
PLNP	4.88±0.1	3.02±0.1	2.50	0.27±0.02	3.96

**Flux of Particles and Rate of Adsorption.** The kinetics governed by the transportation of material to the surface was assessed using SPAR for the first adsorbed CLNP or PLNP layer. To achieve comprehensive information regarding the mechanism of adsorption, a comparison between the initial rate and rate of molecular arrival at the interface (given by theoretical flux,  $J$ ) is discussed. The flux  $J$  (at the stagnation point where there is zero hydrodynamic flow)<sup>55</sup> is given by *Dabros* and *van de Ven*<sup>56</sup> according to equation 5:

$$J = k \times \nu^{1/3} \times D^{2/3} \times C_b \quad [5]$$

Flux  $J$  is dependent on the transport coefficient  $k$ , kinematic viscosity ( $\nu$ ),  $D$  (diffusion coefficient of the molecule) and  $C_b$  (concentration of molecules in bulk solution). The final flux  $J$  is calculated to be 0.0833 mg/m<sup>2</sup>s for CLNPs and 0.115 mg/m<sup>2</sup>s for PLNPs (explained in the supplementary material and Figure S7). The higher flux achieved by PLNPs indicates the existence of a lower

energy barrier or a more energetically favorable interaction in the case of longer grafted chains of the arriving PLNP at the interface.<sup>57</sup>

In the initial stage of the adsorption process, if all arriving particles at the interface adsorb, the initial adsorption rate  $(\frac{d\Gamma}{dt})_0$  will be equal to the flux.  $Q_n$  (i.e., quality factor) is used to determine this slope  $(\frac{d\Gamma}{dt})_{t=0}$  according to equation 6:

$$\Gamma_{t=0} = Q_n \times \frac{\Delta S}{S_0} \quad [6]$$

The slope of the initial adsorption is shown in Figure S8. Slopes of 0.017 mg/m<sup>2</sup>s for CLNPs and 0.025 mg/m<sup>2</sup>s for PLNPs were observed and are significantly lower than the final flux  $J$ . This implies that approximately 20% of CLNPs and 22% of PLNPs arriving at the PAH interface would be adsorbed in the real scenario. There is no doubt that particle size and nanoparticle packing behavior (including localization/distribution/reorientation) of adsorbing molecules play important roles.<sup>58</sup> This means that the larger PLNPs with longer grafted side chains had a greater affinity towards the PAH-coated surface.

### **Significance and Novelty**

The importance of matching the lignin functions to the target application is frequently undervalued in the literature. In this study, we produced bamboo-based lignin nanoparticles with tunable negative charges and grafted side chain lengths for the first time. We showed that the grafted side chain length influences the assembly of the nanoparticles and their adsorption to the liquid-solid interface. These novel functional lignin nanoparticles would offer some economical and environmental advantages applied in coating, glue, and composite material production based on the following features: 1) cost-effective one-step nanoparticle preparation method compared to previous reports,<sup>18-20,59</sup> since aqueous acid-precipitation rather than solvent systems was used for lignin nanoparticle production, 2) high stability over an extended pH range of 5-11 (Figure 3b), 3)

high tolerance against ionic strength (Figure 3c), 4) control over the size (Figure 3b) and functionality (Table 1) of the nanoparticles, 5) excellent pH-responsive recyclability (Figure 2b) and 6) strong interaction towards polyelectrolytes (Figure 4).

## CONCLUSION

We fabricated functional lignin nanoparticles with different grafted chain lengths and sizes via a simple acid-precipitation process using carboxymethylated and carboxypentylated lignin. Carboxypentylated lignin formed larger nanoparticles due to the dynamic properties of the longer alkyl side chain. The nanoparticles demonstrated great pH reversibility response, salt tolerance, and stability at a wide pH range. We showed that these particles can be used in a layer-by-layer assembly using cationic polyelectrolytes. PLNPs resulted in a greater adsorbed amount compared to CLNPs, owing to the flexibility of the pentyl chain on PLNPs. Adsorption studies illustrated an inverse relation between trapped water and adsorbed mass, with PLNP adsorption of  $\Gamma=3.02$  mg/m<sup>2</sup> and  $x_{\text{trapped water}}=0.27$  mg/mg, and the CLNP adsorption of  $\Gamma=2.51$  mg/m<sup>2</sup> and  $x_{\text{trapped water}}=0.3$  mg/mg. The flux of adsorption demonstrated the dependence of adsorption on the particle size and nanoparticle packing behavior, where approximately 20% of arriving nanoparticles were adsorbed on the PAH interface.

The practical benefit of this study is the precise control over nanoparticle size and how they can be tuned for the design of multilayer assemblies. Applications of the functional lignin nanoparticles range from composites to drug delivery where the adsorption behavior of particles is designed to obtain a specific multilayer matrix. Biological compatibility studies and antimicrobial properties of nanoparticles will be carried out in future studies.

## ASSOCIATED CONTENT

### Supporting Information

Proposed carboxyalkylation reaction scheme, Phosphitylation reaction, and  $^1\text{H}$   $^1\text{H}$  COSY NMR spectra of carboxymethylated lignin (Figure S1), Overview of parameters in the optical model at the interface (Figure S2); Lignin nanoparticle formation, Particle size variation as a function of lignin concentration, Dispersion stability of LNPs as a function of pH, and Particle size of LNPs in pH-responsive reversibility analysis (Figure S3); TEM image of LNPs (Figure S4); Effect of salt on zeta potential of nanoparticles, Effect of time on hydrodynamic diameter (Figure S5); Frequency change of multilayer CLNPs and PLNPs with PAH (Figure S6); Dimensionless  $\alpha$  as a function of Reynolds number (Figure S7); SPAR initial adsorption ( $\frac{d\Gamma}{dt}$ ) of CLNP and PLNP on PAH (Figure S8); Charge density and molecular weight of samples (Table S1).

## **AUTHOR INFORMATION**

### **Corresponding Author**

\* E-mail: pfatehi@lakeheadu.ca. Tel: 807-4343-8697. Fax: 807-346-7943.

### **Author Contributions**

The research was conceived by NA and PF. The manuscript was written by NA in close collaboration with TB and with contributions from the other co-authors. NA conducted the experimental analysis in co-operation with LW and TB. XW, CX, LW, and PF are the principal scientists of this work. The authors have approved the final version of the manuscript.

### **Funding**

The authors would like to acknowledge Globalink MITACS national research organization, NSERC, Canada Foundation for Innovation, Canada Research Chairs, Northern Ontario Heritage Fund Corporation, and Ontario Research Fund programs for supporting this research.

## **ACKNOWLEDGMENT**

The authors would like to acknowledge the Electron microscopy laboratory of the University of Turku, Finland, for TEM imaging of this work. This work is also part of the activities within Johan Gadolin Process Chemistry Centre at Åbo Akademi University and the Department of Fiber and Polymer Technology at KTH Royal Institute of Technology during a joint project with Green Processes Research Centre of Lakehead University. Lars Wågberg and Tobias Bensefelt also acknowledge the Knut and Alice Wallenberg Research Foundation through WWSC (Wallenberg Wood Science Centre).

## REFERENCE

- (1) Zakzeski, J.; Bruijninx, P.C.A.; Jongerius, A.L.; Weckhuysen, B.M. The catalytic valorization of lignin for the production of renewable chemicals. *Chem. rev.* **2010**, *110*, 3552-3599.
- (2) Nascimento, D.M.; Nunes, Y.L.; Figueiredo, M.C.B.; de Azeredo, H.M.C.; Aouada, F.A.; Feitosa, J.P.A.; Rosa, M.F.; Dufresne, A. Nanocellulose nanocomposite hydrogels: technological and environmental issues. *Green Chem.* **2018**, *20*, 2428-2448.
- (3) Zhao, W.W.; Simmons, B.; Singh, S.; Ragauskas, A.J.; Cheng, G. From lignin association to nano-/micro-particle preparation: Extracting higher value of lignin. *Green Chem.* **2016**, *18*, 5693–5700.
- (4) Duval, A.; Lawoko, M. A review on lignin-based polymeric, micro- and nano-structured materials. *React. Funct. Polym.* **2014**, *85*, 78–96.
- (5) Hambarzumyan, A.; Foulon, L.; Bercu, N.B.; Pernes, M.; Maigret, J.E.; Molinari, M.; Chabbert, B.; Aguié-Beghin, V. Organosolv lignin as natural grafting additive to improve the water resistance of films using cellulose nanocrystals. *Chem. Eng. J.* **2015**, *264*, 780-788.

- (6) Zhang, Y.; Xu, W.; Wang, X.; Ni, S.; Rosqvist, E.; Smått, J.H.; Peltonen, J.; Hou, Q.; Qin, M.; Willför, S.; Xu, C. From biomass to nanomaterials: A green procedure for preparation of holistic bamboo multifunctional nanocomposites based on formic acid rapid fractionation. *ACS Sustain. Chem. Eng.* **2019**, *7*, 6592-6600.
- (7) Sipponen, M.H.; Lange, H.; Ago, M.; Crestini, C. Understanding lignin aggregation processes. A case study: budesonide entrapment and stimuli controlled release from lignin nanoparticles. *ACS Sustain. Chem. Eng.* **2018**, *6*, 9342-9351.
- (8) Chen, N.; Dempere, L.A.; Tong, Z. Synthesis of pH-responsive lignin-based nanocapsules for controlled release of hydrophobic molecules. *ACS Sustain. Chem. Eng.* **2016**, *4*, 5204-5211.
- (9) Li, Y.; Wu, M.; Wang, B.; Wu, Y.; Ma, M.; Zhang, X. Synthesis of magnetic lignin-based hollow microspheres: a highly adsorptive and reusable adsorbent derived from renewable resources. *ACS Sustain. Chem. Eng.* **2016**, *4*, 5523-5532.
- (10) Luo, X.; Liu, C.; Yuan, J.; Zhu, X.; Liu, S. Interfacial solid-phase chemical modification with Mannich reaction and Fe (III) chelation for designing lignin-based spherical nanoparticle adsorbents for highly efficient removal of low concentration phosphate from water. *ACS Sustain. Chem. Eng.* **2017**, *5*, 6539-6547.
- (11) Klapiszewski, L.; Bartczak, P.; Wysokowski, M.; Jankowska, M.; Kabat, K.; Jesionowski, T. Silica conjugated with kraft lignin and its use as a novel 'green' sorbent for hazardous metal ions removal. *Chem. Eng. J.* **2015**, *260*, 684-693.
- (12) Leskinen, T.; Witos, J.; Valle-Delgado, J.J.; Lintinen, K.; Kostianen, M.; Wiedmer, S.K.; Österberg, M.; Mattinen, M.L. Adsorption of proteins on colloidal lignin particles for advanced biomaterials. *Biomacromolecules*, **2017**, *18*, 2767-2776.

- (13) Österberg, M.; Sipponen, M.H.; Mattos, B.D.; Rojas, O.J. Spherical lignin particles: a review on their sustainability and applications. *Green Chem.* **2020**, *22*, 2712-2733.
- (14) Gao, W. Fatehi, P. Lignin for polymer and nanoparticle production: Current status and challenges. *Canadian J. Chem. Eng.* **2019**, *97*, 2827-2842.
- (15) Frangville, C.; Rutkevicius, M.; Richter, A.P.; Veleev, O.D.; Stoyanov, S.D.; Paunov, V.N. Fabrication of environmentally biodegradable lignin nanoparticles. *ChemPhysChem*, **2012**, *13*, 4235.
- (16) Richter, A.P.; Brown, J.S.; Bharti, B.; Wang, A.; Gangwal, S.; Houck, K.; Hubal, E.A.C.; Paunov, V.N.; Stoyanov, S.D.; Veleev, O.D. An environmentally benign antimicrobial nanoparticle based on a silver-infused lignin core. *Nat. Nanotechnol.* **2015**, *10*, 817-823.
- (17) Chen, L.; Zhou, X.; Shi, Y.; Gao, B.; Wu, J.; Kirk, T.B.; Xu, J.; Xue, W. Green synthesis of lignin nanoparticle in aqueous hydrotropic solution toward broadening the window for its processing and application. *Chem. Eng. J.* **2018**, *346*, 217-225.
- (18) Richter, A.P.; Bharti, B.; Armstrong, H.B.; Brown, J.S.; Plemmons, D.; Paunov, V.N.; Stoyanov, S.D.; Veleev, O.D. Synthesis and characterization of biodegradable lignin nanoparticles with tunable surface properties. *Langmuir*, **2016**, *32*, 6468-6477.
- (19) He, X.; Luzi, F.; Yang, W.; Xiao, Z.; Torre, L.; Xie, Y.; Puglia, D. Citric acid as green modifier for tuned hydrophilicity of surface modified cellulose and lignin nanoparticles. *ACS Sustain. Chem. Eng.* **2018**, *6*, 9966-9978.
- (20) Qian, Y.; Zhang, Q.; Qiu, X.; Zhu, S. CO<sub>2</sub>-responsive diethylaminoethyl-modified lignin nanoparticles and their application as surfactants for CO<sub>2</sub>/N<sub>2</sub>-switchable Pickering emulsions. *Green Chem.* **2014**, *16*, 4963-4968.

- (21) Tariq, M.; Serro, A.P.; Colaco, R.; Saramago, B.; Lopes, J.N.C.; Rebelo, L.P.N. Effect of alkyl chain length on the adsorption and frictional behaviour of 1-alkyl-3-methylimidazolium chloride ionic liquid surfactants on gold surfaces. *Colloids Surf. A: Physicochem. Eng. Asp.* **2011**, *377*, 361-366.
- (22) Hassan, S.; Duclaux, L.; Leveque, J.M.; Reinert, L.; Farooq, A.; Yasin, T. Effect of cation type, alkyl chain length, adsorbate size on adsorption kinetics and isotherms of bromide ionic liquids from aqueous solutions onto microporous fabric and granulated activated carbons. *J. Environ. Manage.* **2014**, *144*, 108-117.
- (23) Erdmenger, T.; Vitz, J.; Wiesbrock, F.; Schubert, U.S. Influence of different branched alkyl side chains on the properties of imidazolium-based ionic liquids. *J. Mater. Chem.* **2008**, *18*, 5267-5273.
- (24) Spori, D.M.; Venkataraman, N.V.; Tosatti, S.G.P.; Durmaz, F.; Spencer, N.D.; Zurcher, S. Influence of alkyl chain length on phosphate self-assembled monolayers. *Langmuir*, **2007**, *23*, 8053-8060.
- (25) Norgren, M.; Gardlund, L.; Notley, S.M.; Htun, M.; Wågberg, L. Smooth model surfaces from lignin derivatives. II. Adsorption of polyelectrolytes and PECs monitored by QCM-D. *Langmuir*, **2007**, *23*, 3737-3743.
- (26) Galvan, M.V.; Mocchiutti, P.; Cornaglia, L.M.; Zanuttini, M.A. Dual-polyelectrolyte adsorption of poly (allylamine hydrochloride) and xylan onto recycled unbleached kraft pulps. *BioResources*. **2012**, *7*, 2075-2089.
- (27) Buchman, J.T.; Rahnamoun, A.; Landy, K.M.; Zhang, X.; Vartanian, A.M.; Jacob, L.M.; Murphy, C.J.; Hernandez, R.; Haynes, C.L. Using an environmentally-relevant panel of Gram-

negative bacteria to assess the toxicity of polyallylamine hydrochloride-wrapped gold nanoparticles. *Environ. Sci. Nano.* **2018**, *5*, 279-288.

(28) Kishani, S.; Vilaplana, F.; Ruda, M.; Hansson, P.; Wågberg, L. Influence of Solubility on the Adsorption of Different Xyloglucan Fractions at Cellulose--Water Interfaces. *Biomacromolecules*, **2019**, *21*, 772-782.

(29) Kishani, S.; Escalante, A.; Toriz, G.; Vilaplana, F.; Gatenholm, P.; Hansson, P.; Wågberg, L. Experimental and theoretical evaluation of the solubility/insolubility of spruce xylan (arabino glucuronoxylan). *Biomacromolecules*, **2019**, *20*, 1263-1270.

(30) Tribot, A.; Amer, G.; Alio, M.A.; de Baynast, H.; Delattre, C.; Pons, A.; Mathias, J.D.; Callois, J.M.; Vial, C.; Michaud, P.; Dussap, C.G. Wood-lignin: Supply, extraction processes and use as bio-based material. *European Polym. J.* **2019**, *112*, 228-240.

(31) Li, M.F.; Sun, S.N.; Xu, F.; Sun, R.C. Formic acid based organosolv pulping of bamboo (*Phyllostachys acuta*): Comparative characterization of the dissolved lignins with milled wood lignin. *Chem. Eng. J.* **2012**, *179*, 80-89.

(32) Dapía, S.; Santos, V.; Parajó, J.C. Study of formic acid as an agent for biomass fractionation. *Biomass Bioenerg.* **2002**, *22*, 213-221.

(33) Obrocea, P.; Cimpoesu, G. Contribution to sprucewood delignification with peroxyformic acid I. The effect of pulping temperature and time. *Cellulose Chem. Technol.* **1998**, *32*, 517-525.

(34) Zhang, Y.; Qin, M.; Xu, W.; Fu, Y.; Wang, Z.; Li, Z.; Willfor, S.; Xu, C.; Hou, Q. Structural changes of bamboo-derived lignin in an integrated process of autohydrolysis and formic acid inducing rapid delignification. *Ind. Crops Prod.* **2018**, *115*, 194-201.

(35) Konduri, M.K.; Kong, F.; Fatehi, P. Production of carboxymethylated lignin and its application as a dispersant. *Eur. Polym. J.* **2015**, *70*, 371-383.

- (36) Bahrpaima, K.; Fatehi, P. Synthesis and characterization of carboxyethylated lignosulfonate. *ChemSusChem*, **2018**, *11*, 2967-2980.
- (37) Bahrpaima, K.; Fatehi, P. Preparation and coagulation performance of carboxypropylated and carboxypentylated lignosulfonates for dye removal. *Biomolecules*, **2019**, *9*, 383.
- (38) Zheng, X.; Ma, X.; Chen, L.; Cao, S.; Nasrallah, J. Lignin extraction and recovery in hydrothermal pretreatment of bamboo. *J. Biores. Biopro.* **2016**, *1*, 145-151.
- (39) Zhang, Y.; Hou, Q.; Xu, W.; Qin, M.; Fu, Y.; Wang, Z.; Willfor, S.; Xu, C. Revealing the structure of bamboo lignin obtained by formic acid delignification at different pressure levels. *Ind. Crops Prod.* **2017**, *108*, 864-871.
- (40) Dijt, J.C.; Stuart, M.A.C.; Fleer, G.J. Reflectometry as a tool for adsorption studies. *Adv. Colloid Interf. Sci.* **1994**, *50*, 79-101.
- (41) Alipoormazandarani, N.; Fatehi, P. Deposition behavior of lignin on solid surface assessed by stagnation point adsorption reflectometry. *RSC Advances*, 2021.
- (42) Porus, M.; Maroni, P.; Borkovec, M. Structure of adsorbed polyelectrolyte monolayers investigated by combining optical reflectometry and piezoelectric techniques. *Langmuir*, **2012**, *28*, 5642-5651.
- (43) Adamczyk, Z.; Zembala, M.; Warszynski, P.; Jachimska, B. Characterization of polyelectrolyte multilayers by the streaming potential method. *Langmuir*. **2004**, *20*, 10517-10525.
- (44) Dong, D.; Fricke, A.L. Intrinsic viscosity and the molecular weight of kraft lignin. *Polymer*, **1995**, *36*, 2075-2078.
- (45) Brilliantov, N.V.; Kuznetsov, D.V.; Klein, R., Chain collapse and counterion condensation in dilute polyelectrolyte solutions. *Phys. rev. let.* **1998**, *81*, 1433.

- (46) Tang, Q.; Zhou, M.; Li, Y.; Qiu, X.; Yang, D. Formation of uniform colloidal spheres based on liginosulfonate, a renewable biomass resource recovered from pulping spent liquor. *ACS Sustain. Chem. Eng.* **2018**, *6*, 1379-1386.
- (47) Salentinig, S.; Schubert, M. Softwood lignin self-assembly for nanomaterial design. *Biomacromolecules*, **2017**, *18*, 2649-2653.
- (48) Norgren, M.; Edlund, H.; Wågberg, L. Aggregation of lignin derivatives under alkaline conditions. Kinetics and aggregate structure. *Langmuir*, **2002**, *18*, 2859-2865.
- (49) Verwey, E.J.W.; Overbeek, J.T.G. and Van Nes, K. Theory of the stability of lyophobic colloids: the interaction of sol particles having an electric double layer. *J. Phys. Chem.* **1948**, *51*(3), 631-636.
- (50) Smits, R.G.; Kuil, M.E.; Mandel, M. Molar mass and ionic strength dependence of the apparent diffusion coefficient of a flexible polyelectrolyte at dilute and semidilute concentrations: Linear poly (ethylenimine). *Macromolecules*, **1993**, *26*, 6808-6816.
- (51) Wågberg, L.; Decher, G.; Norgren, M.; Lindström, T.; Ankerfors, M.; Axnäs, K. The build-up of polyelectrolyte multilayers of microfibrillated cellulose and cationic polyelectrolytes. *Langmuir*, **2008**, *24*, 784-795.
- (52) Adamczyk, Z.; Warszyński, P., Role of electrostatic interactions in particle adsorption. *Adv. Colloid Interface Sci.* **1996**, *63*, 41-149.
- (53) Engström, J.; Bensefelt, T.; Wågberg, L.; D'Agosto, F.; Lansalot, M.; Carlmark, A.; Malmström, E. Tailoring adhesion of anionic surfaces using cationic PISA-latexes—towards tough nanocellulose materials in the wet state. *Nanoscale*, **2019**, *11*, 4287-4302.
- (54) Dejeu, J.; Buisson, L.; Guth, M.C.; Roidor, C.; Membrey, F.; Charrat, D.; Foissy, A. Early steps of the film growth mechanism in self-assembled multilayers of PAH and PSS on silica:

polymer uptake, charge balance and AFM analysis. *Colloids Surf. A Physicochem. Eng. Asp.* **2006**, 288, 26-35.

(55) Iruthayaraj, J.; Poptoshev, E.; Vareikis, A.; Makuska, R.; van der Wal, A.; Claesson, P.M. Adsorption of low charge density polyelectrolyte containing poly (ethylene oxide) side chains on silica: Effects of ionic strength and pH. *Macromolecules*, **2005**, 38, 6152-6160.

(56) Dabroś, T. van de Ven, T. G. A direct method for studying particle deposition onto solid surfaces. *Colloid Polym. Sci.* **1983**, 261, 694-707.

(57) Weroński, P.; Elimelech, M. Novel numerical method for calculating initial flux of colloid particle adsorption through an energy barrier. *J. colloid interface sci.* **2008**, 319, 406-415.

(58) Staszak, M. A linear diffusion model of adsorption kinetics at fluid/fluid interfaces. *J. Surfactants Deterg.* **2016**, 19, 297-314.

(59) Ago, M.; Huan, S.; Borghei, M.; Raula, J.; Kauppinen, E.I.; Rojas, O.J. High-throughput synthesis of lignin particles (~ 30 nm to ~ 2 mm) via aerosol flow reactor: Size fractionation and utilization in pickering emulsions. *ACS Appl. Mater. Interf.*, **2016**, 8, 23302-23310.

## Table of Content (TOC)

